Chinese Journal of Oceanology and Limnology
Vol. 28 No. 5, P. 1055-1067, 2010
DOI: 10.1007/s00343-010-0035-x

Pathways of mesoscale variability in the South China Sea*

ZHUANG Wei (庄伟)[1,**], DU Yan (杜岩)[1], WANG Dongxiao (王东晓)[1], XIE Qiang (谢强)[1], XIE Shangping (谢尚平)[2, 3]

[1] *Key Laboratory of Tropical Marine Environmental Dynamics, South China Sea Institute of Oceanology, Chinese Academy of Sciences, Guangzhou 510301, China*

[2] *International Pacific Research Center and Department of Meteorology, University of Hawaii, Honolulu 96822, Hawaii, USA*

[3] *Physical Oceanography Laboratory, Ocean University of China, Qingdao 266100, China*

Received Jan. 29, 2010; revision accepted Jun. 2, 2010

Abstract The propagation of oceanic mesoscale signals in the South China Sea (SCS) is mapped from satellite altimetric observations and an eddy-resolving global ocean model by using the maximum cross-correlation (MCC) method. Significant mesoscale signals propagate along two major bands of high variability. The northern band is located west of the Luzon Strait, characterized by southwestward eddy propagation. Although eddies are the most active in winter, their southwestward migrations, steered by bathymetry, occur throughout the year. Advection by the mean flow plays a secondary role in modulating the propagating speed. The southern eddy band lies in the southwest part of the SCS deep basin and is oriented in an approximately meridional direction. Mesoscale variability propagates southward along the band in autumn. This southward eddy pathway could not be explained by mean flow advection and is likely related to eddy detachments from the western boundary current due to nonlinear effects. Our mapping of eddy propagation velocities provides important information for further understanding eddy dynamics in the SCS.

Keyword: sea level; mesoscale variability; maximum cross-correlation; South China Sea (SCS)

1 INTRODUCTION

The South China Sea (SCS) is a semi-enclosed marginal sea of the western Pacific, connecting in the south with Java Sea through the Karimata Strait and in the northeast with the Pacific through deep Luzon Strait (Fig.1). The bathymetry of the SCS is complex, with a deep basin in the center elongating in the northeast-southwest direction and numerous islands and reefs around the basin. The climate of SCS is part of the East Asian monsoon system (Wyrtki, 1961). Driven by monsoonal winds, oceanic circulation in the upper layer exhibits strong seasonal variability, predominantly cyclonic in winter and anticyclonic in summer (Liu et al., 2001b; Wang et al., 2003a). In the northern SCS (NSCS), circulation is greatly affected by the Kuroshio intrusion (e.g. Shaw, 1991), which appears to be a transient phenomenon related to interaction between the Kuroshio and eddies (Jia et al., 2005; Yuan et al., 2006). However, the dynamical interior is still not fully understood.

Mesoscale fluctuations on temporal-spatial scales between 20–150 days and 50–500 km dominate the oceanic variability (Wyrtki et al., 1976; Richman et al., 1977) and are largely accounted for by eddies (Chelton et al., 2007). Besides seasonal variability, circulation in the SCS also displays energetic mesoscale variability (MV). Multi-scale eddies embedded in the circulation have been observed from different hydrographic datasets (Chu et al., 1998; Xu et al., 1982) and reproduced by eddy-resolving numerical models (Gan et al., 2006; Metzger, 2003). The application of satellite altimetry has significantly enhanced our understanding of MV in the SCS. Based on along-track altimetry data, high MV in the SCS was considered to be along two bands north of 10°N: a stronger one lies along the northwestern boundary west of the Luzon Strait, and a weaker

* Supported by the Knowledge Innovation Program of the Chinese Academy of Sciences (KZCX1-YW-12-01), the National Natural Science Foundation of China (Nos. 40806006, 40876009), the Knowledge Innovation Program of the Chinese Academy of Sciences (No. KZCX2-YW-BR-04), the Qianren Project

** Corresponding author: zhuang@scsio.ac.cn

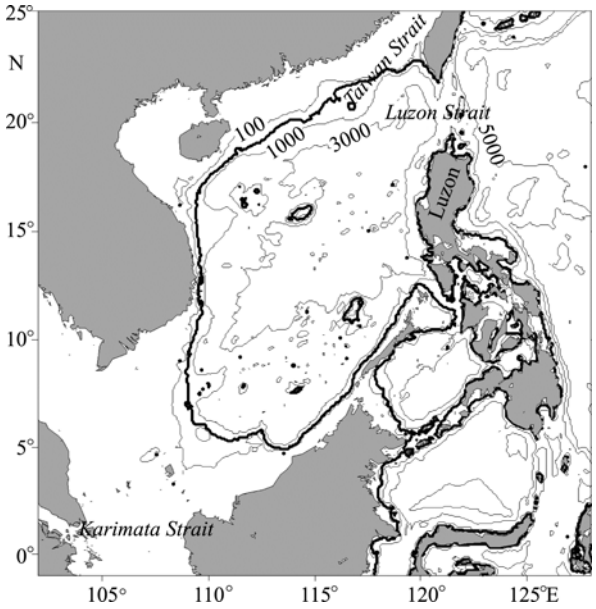

Fig.1 Bottom topography of the South China Sea derived from the ETOPO5, with the 100, 200, 1000, 3000 and 5000 m isobaths shown

The bold contours represent the 200 m isoline

one is in a NE-SW direction across the central basin (Wang et al., 2000). Propagations of MV have been widely observed in the SCS. Using buoy and altimetry observations, Liu et al. (2001a) noted the importance of eddy movements to intraseasonal variability of the thermocline in the central SCS. Combination of satellite observations and model simulations indicates that intraseasonal sea level variations in the deep basin are mainly attributed to flow instabilities and tend to propagate along high-variance bands (Zhuang et al., 2010). The geographic distributions and tracks of eddies were depicted first based on a merged altimetry dataset by Wang et al. (2003b). Following this work, Xiu et al. (2010) recently described various eddy characteristics in the SCS using numerical study and showed the westward tendency of eddy trajectories.

Near the Luzon Strait, Li et al. (1998) recorded the evidence of anticyclonic eddies in the NSCS and treated these eddies as Kuroshio origin. Although strong 3–6-month MV exists in both the NSCS and the western Pacific (Hu et al., 2001), the Kuroshio appears to act as a barrier to westward propagation of MV from the Pacific, and only 45-day MV could enter the SCS via the Luzon Strait (Li et al., 2007). Investigations by Wu et al. (2007) also showed that the westward propagating eddies in the NSCS originate near the Luzon Strait rather than coming from the western Pacific. These studies improved our understanding of transient MV and associated eddy activities in the SCS.

Despite the above studies on the movements of MV and eddies, a general pattern of MV propagations in the SCS has not been given. Previous studies on the movement of eddies are based on visual tracking of identifiable features of sea surface height (SSH) maps in time sequences (Wang et al., 2003b; Xiu et al., 2010). Extending previous studies on Lagrangian tracking of individual eddies, this research applies a space-time lag correlation technique to provide a high-resolution Eulerian description of eddy pathways, which is accomplished by using merged altimetry data and the simulations of an eddy-resolving ocean general circulation model (OGCM). The results show the important effects of wave propagation, mean circulation, bathymetry and nonlinear processes. The paper is organized as follows. Section 2 describes observational data and model outputs, and introduces briefly new approach in estimating propagation velocity. Section 3 presents the annual and seasonal pathways of mesoscale signals. Discussion and conclusion are provided in Sections 4 and 5, respectively.

2 DATA AND METHODS

2.1 Observational data

Sea level anomalies (SLAs) have been measured by multi-satellite altimeters for more than a decade. Estimation of mesoscale signals is greatly improved when data from two satellites are processed with the use of an objective mapping technique (Ducet et al., 2000). Compared to the results obtained with the two altimeters, MV estimated with four satellites shows little improvement for low latitudes, where the size of typical structures is relatively large (Pascual et al., 2006). It is known that altimetry measurements could be contaminated by high-frequency (HF) variability at periods shorter than the Nyquist period of the altimetric repeat cycle. These unresolved HF signals are mainly tides (Schlax et al., 1994) or barotropic variability induced by HF atmospheric forcing (Fukumori et al., 1998). In 2005, data set of multi-mission altimeter were updated with new corrections using an up-to-date tidal model (GOT2000, Goddard/Grenoble Ocean Tide) and a new barotropic model (MOG2D-G, Modèle aux Ondes de Gravité 2-Dimensions Global), which largely suppressed the HF aliasing signals (Carrère et al., 2003, Lyard et al., 2006).

In this study, we use the newly released altimetry dataset. Volkov et al. (2007) compared the new version with previous altimetry products and found

that it makes much better tidal and atmospheric barometric corrections. The improved accuracy enabled the study of MV even over some continental shelves. To keep the sampling homogeneous for this study, we adopt the merged SLA data derived from simultaneous measurements of two satellites (Topex/Poseidon or Jason-1 + ERS or Envisat). The product was distributed by AVISO. It consists of maps since October 1992 with 7-day time intervals and Mercator 1/3° spatial resolution. Data from 2000–2008 are analyzed to compare with the OGCM simulations. To avoid possible residual aliasing, the data over the shelves shallower than 100 m are masked out in the figures.

To show basin-scale geostrophic currents, we use the absolute dynamic topography (ADT), which consists of a mean dynamic topography (MDT) and the altimetric SLAs. The method on the estimation of MDT was introduced by Rio et al. (2005). The ADT data were also distributed by AVISO with the same resolution as SLAs. The ADT represents sea level above the geoid, while the simulated free surface is referred to global mean SSH. Within the SCS domain, regional annual mean values of ADT and simulated SSH are 229.9 and 62.3 cm, respectively. Their difference (167.6 cm) is subtracted from ADT for easy viewing and comparisons. Such an adjustment does not change the spatial gradient of ADT and the associated geostropic currents.

2.2 Product from the eddy-resolving model

The satellite observations are compared with the product from an eddy-resolving OGCM for the Earth Simulator (OFES; Masumoto et al., 2004). The model is based on the Modular Ocean Model (MOM3; Pacanowski et al., 2000), with a near-global domain extending from 75°S to 75°N. Horizontal resolution is 0.1°×0.1°. There are 54 vertical *Z*-coordinate levels, with varying resolutions from 5 m at the surface to 330 m at the maximum depth of 6 065 m.

Following a 50-year spin-up integration with monthly climatological forcings, a hindcast simulation from 1950–2005 was conducted with surface wind stress, heat and freshwater fluxes derived from the daily mean NCEP/NCAR reanalysis (NCEP run hereafter). In addition, sea surface salinity was restored to the monthly climatology of World Ocean Atlas 1998. Another hindcast run started from the NCEP run on July 20, 1999, but was forced by daily mean surface wind stress from QuikSCAT measurements (QSCAT run). Other atmospheric forcings were the same as those in the NCEP run (Sasaki et al., 2006). This study uses the output of QSCAT run, whose performance is better than the NCEP run because of high resolution and accuracy of the wind forcing (Zhuang et al., 2010). Three-day snapshots of SSH during 2000–2008 are applied in this study.

To extract MV, the annual and semiannual cycles are removed first using a harmonic filter. This is done because the cycles are not induced mainly by eddy activities but by direct atmospheric forcings including Ekman pumping, wind stirring, and cooling convection (Qu et al., 2007). To examine the significant periods of the residual signals, we select two locations (denoted with green triangles in Fig.3a) where eddy often occurs (Xiu et al., 2010), and analyze the power spectra of residual SSH. The results of both altimetry and OFES indicate that the 30–180 days signals are often above the 95% confidence level, while other signals in lower and higher frequencies are insignificant at the 95% level (Fig.2). Considering different temporal resolutions for altimeter and OFES data (7 and 3 days, respectively), we select their common multiples (21 and 175 days) as the cutoff periods. Thus, a 21–175 days band-pass filter is used to remove low-frequency variability and suppress synoptic disturbances with periods shorter than 20 days. An additional harmonic filter is then applied to remove possible tidal aliasing near 60 days (Li et al., 2007). This frequency band is similar to the MV definition by Wang et al. (2000), except that they had to remove all signals shorter than 60 days due to strong tidal aliasing in previous altimetry products.

2.3 Maximum cross-correlation technique

The maximum cross-correlation (MCC) method is a space-time lagged technique for detecting translational motions from time-sequential remote sensing data and has been commonly used to estimate motion velocities of some spatial or temporal features (Domingues et al., 2000; Emery et al., 1986; Fu, 2006). This method is used to estimate the speed and direction of mesoscale signals in this study. At a given location (x_0, y_0), the cross- correlations of sea level MV with neighboring sea level MV within a certain range are calculated for some time lags. At each time lag (ΔT), the position of maximum correlation is identified and a velocity could be estimated from the time lag and the distance (Δx, Δy) of the position from the origin. An average velocity vector (u, v) weighted by correlation coeffi-

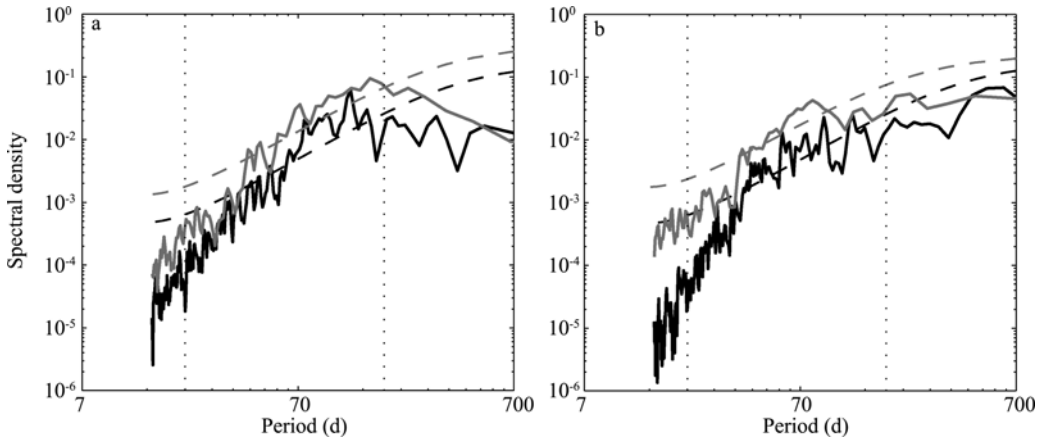

Fig.2 Power spectra of SLAs derived from altimeter observations (black line) and OFES simulations (gray line) in zones with high eddy occurrences

a. south of the NSCS continental slope; b. east of the Vietnam coast. The annual and semiannual harmonics have been removed from the SLAs. Dashed lines and dotted lines represent the 95% confidence level and cutoff periods for mesoscale signals. The positions selected for spectrum analysis are shown as green triangles in Fig.3a

cients is then calculated from the estimates at various time lags as:

$$(u(x_0, y_0), v(x_0, y_0)) = \frac{\sum_i (\Delta x_i/\Delta T_i, \Delta y_i/\Delta T_i) C_i}{\sum_i C_i}$$

where C_i is the maximum correlation at ΔT_i, and Δx_i, Δy_i represent the distance between the location of maximum correlation and the origin. The average velocity is assigned to the propagation velocity of MV at the given grid (x_0, y_0).

To focus on mesoscale properties and to reduce incidence of spurious MCC vectors, the maximum possible velocity is set at 26 km/day (30 cm/s), which is generally larger than the propagation speeds of eddies (Chelton et al., 2007). Meanwhile, the phase speeds of baroclinic Rossby waves in the SCS are mostly lower than 30 cm/s as well (Gan et al., 2001). The only exception exists in the southeast basin where, as will be shown later, has weak MV and is dynamically unimportant to this study. Therefore, movements of most MV could be well captured under this speed limitation. The area involved in the computation broadens with increasing time lags to meet the velocity limit. The minimum acceptable correlation coefficient should be above the 95% confidence level on the basis of *t*-test. The time lags are limited to less than 42 days. At larger time lags, many correlation coefficients are below the 95% confidence level. In this study, four seasons are defined as follows: winter (December–February), spring (March–May), summer (June–August), and autumn (September–November). Apparently, when calculating velocities in each season, the time series are not smoothly connected. We treat each continuous 3 months (1 season in a specific year) as a group for all time series. In the calculation of lead-lag correlation between two time series, only the data in the same groups are involved in the comparison.

3 RESULTS

3.1 Annual mean pattern

Displayed in color shading in Fig.3a is the standard deviation of sea level MV measured by the satellite altimeters, showing the annual mean intensity of eddy variability. The MV is weak in the southeastern basin and forms two strong bands in the northern and western SCS. The northern high-variance band west of the Luzon Strait is also observed by Wang et al. (2000). The southern one is located near the western SCS, instead of being oriented in the northeast-southwest direction across the basin as marked in Wang et al. (2000). The discrepancy is probably due to the low resolution of single satellite measurements in Wang et al. (2000), especially in the cross-track direction. East of the Luzon Strait, large MV is also observed. The high-variance zones in the western Pacific and the NSCS are not continuous but separated by low values at the Luzon Strait. The distribution is consistent with the eddy occurrence areas estimated by Xiu et al. (2010) and similar to the intraseasonal variance of SSH in deep waters, a sign of eddy activities (Zhuang et al., 2010). Superimposed on the variance fields are the propagation velocities of mesoscale signals. Within two high-variance bands in the interior SCS, vectors are mainly oriented southwestward, suggesting eddy propagations along both bands. The

band orientation and velocity directions match better in the northern band than in the southern one. Away from energetic zones, essentially westward propagations of MV signals are found in the region north of 12°N, in good agreement with trajectories of eddies originating west of the Luzon Island (Wang et al., 2003b). Around the Nansha Islands (east of 112°E, 6°N–12°N), the MV is the weakest and the propagation trend becomes ambiguous. Generally, OFES simulations reproduce not only the mesoscale variances of SSH but also their propagating features (Fig.3b). A difference in the variance pattern exists near 111°E, 14°N, where the observed active MV center is not captured by OFES. As will be shown in Section 3.2, this disagreement mainly results from a difference during spring to summer.

To illustrate the effects of mean flow on eddy propagations, we superimpose the MV propagation velocity on the ocean dynamic topography (Fig.3c, d). In the western Pacific, westward propagations dominate the vast region east of 128°E. Toward the western boundary, propagation velocities are significantly affected by the Kuroshio and Mindanao Current. The vectors bifurcate into two branches at 13°N–14°N and eddies are carried northward/southward by the Kuroshio/Mindanao Current. The majority of northern branch leaps across the Luzon Strait to the east of Taiwan Island. There is no direct westward signal propagation through the Luzon Strait. Only a few vectors show weak northwestward trends into the SCS, following the path of the Kuroshio. In the interior SCS, the annual mean circulation is a weak cyclonic gyre occupying the northern basin. To the south of the NSCS continental slope, the mesoscale signals show obvious migrations along 200–2 000 m isobaths from the southwest of Taiwan Island toward the western SCS, suggesting the steering effects of the bathymetry.

To further clarify eddy propagations near the Luzon Strait and the NSCS, we select a strip along the northern energetic band and extend it across the Luzon Strait to the Pacific (shown as dashed line in Fig.3a). The meridionally averaged velocities along the strip show westward propagations on both sides of the strait (Fig.4a, b). However, propagation velocities diminish to nearly zero at 122°E and 121°E

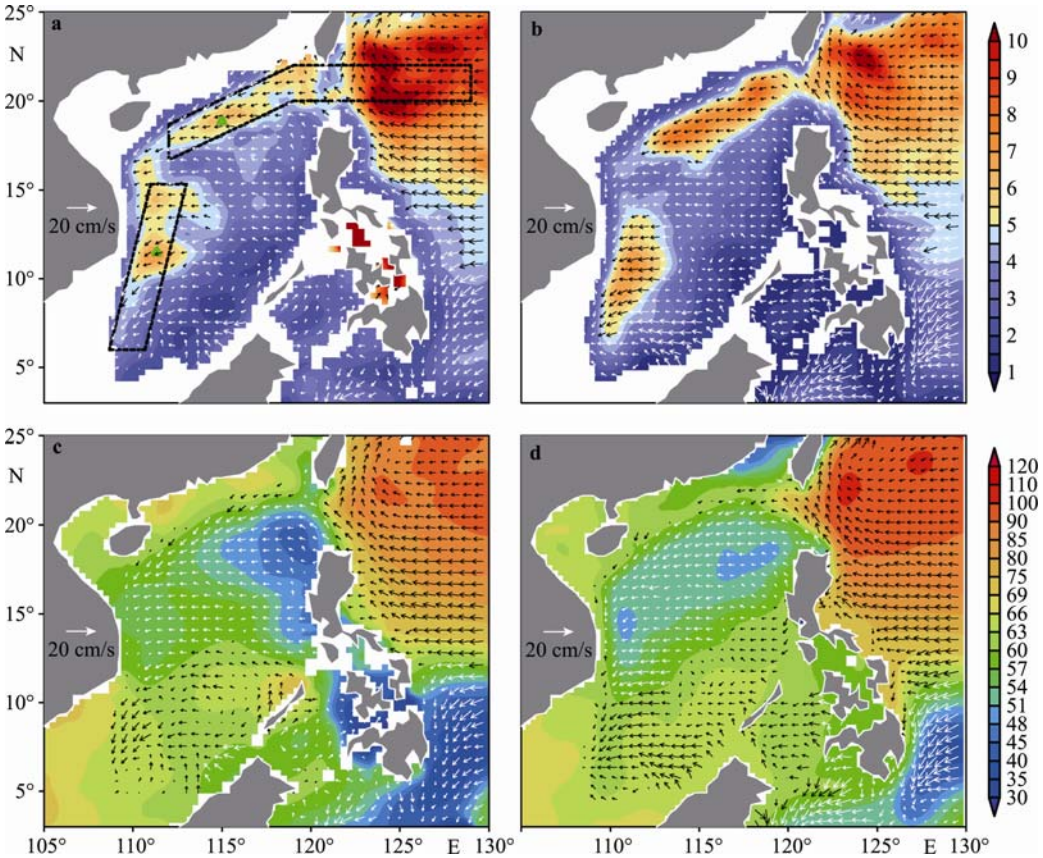

Fig.3 Annual mean standard deviation of sea level mesoscale signals (color shading, unit: cm) and propagation velocities of the signals (vectors) derived from (a) altimeter observations; (b) OFES simulations. (c) The same vectors as (a) superimposed on the annual mean ADT (unit: cm). (d) The same vectors as (b) superimposed on the annual mean SSH from OFES (unit: cm). The two colors of the arrows are shown for easy viewing

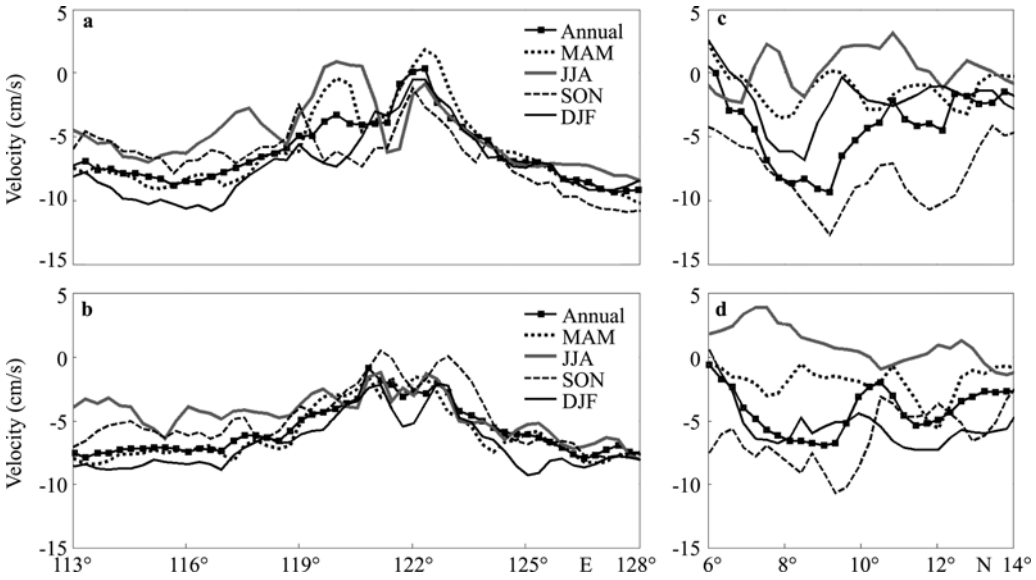

Fig.4 Propagation velocities of mesoscale signals along two strips

a. altimeter observations along the northern band; b. OFES simulations along the northern band; c. altimeter observations along the southern band; d. OFES simulations along the southern band. The strips are shown as dashed lines in Fig.3a. The velocities are parallel to the strips and averaged in the meridional direction for the northern strip and in the zonal direction for the southern strip

in the observations and simulations, respectively. This suggests that directly westward propagation from the Pacific to the NSCS is not significant (Li et al., 2007).

In the southern high-variance band, the energetic MV signals do not move eastward along the path of mean flow but propagate southwestward (Fig.3c, d), probably due to ocean adjustments discussed in the next section. To the east of the Vietnam coast, low propagation velocities are found at the latitudes of 10°N–15°N, associated with a weak annual mean western boundary current.

3.2 Seasonal variations

A pronounced seasonal cycle of SCS circulation and its forcing mechanisms have been studied for decades. Fig.4 reveals that eddy propagations along both high-variance bands also exhibit obvious seasonality. Along the northern band, the propagation of MV keeps westward throughout the year. The observed results (Fig.4a) show that, despite clear spatial variations, mean along-band speed between 111°E–119°E peaks in winter (8.7 cm/s), decreases during spring (7.9 cm/s), reaches the minimum in summer (5.4 cm/s) and then increases during autumn (6.2 cm/s). The OFES hindcast captures this seasonality with corresponding velocities at 8.4, 7.2, 4.2, and 5.9 cm/s, respectively (Fig.4b). Along the southern band, eddy propagations exhibit more significant seasonal variability (Fig.4c, d). Both observations and simulations suggest that, averaged between 6°N–14°N, the southward movement of MV moves fast in autumn (8.1 cm/s and 6.5 cm/s), slows down from winter (2.3 cm/s and 5.4 cm/s) to spring (1.4 cm/s and 1.9 cm/s) and turns northward even slower in summer (0.4 cm/s and 1.0 cm/s). South of 10.5°N, the observations and simulations display similar seasonality. However at 10.5°N−14°N, the simulated speed in autumn is lower than that in winter. To further elucidate the above seasonal characteristics, whole propagation maps in each season are presented here, together with MV amplitudes and mean dynamic heights.

During winter, basin-scale circulation is cyclonic. The lowest SSH is located northwest off the Luzon Island (Fig.5c, d). Associated with strong mean flow, eddy propagations along the northern band are the quickest and the mesoscale variance also reaches its maximum (Fig.5a, b). Along the southern band, MV is relatively weaker, which is the remnant of strong variability in autumn. The simulated MV is stronger in amplitude and propagates faster than the observation (Figs.5a–d). The overestimate of MV in OFES is possibly due to the undervaluation of dissipation rate in the model. In the eastern SCS, Wang et al. (2008) argued that, during the winter monsoon, orographic wind jets spin up alternating clusters of cyclonic and anticyclonic eddies. The vectors in Fig.5 suggest that local eddy energy driven

by Ekman pumping tends to propagate westward under the beta effect, resulting in low MV to the west of Luzon Island.

Circulation in spring turns weaker due to decay of the northeast monsoon. There exists a cyclonic gyre only to the northwest of Luzon Island (Fig.6c, d). MV along the northern band weakens somewhat but is still active (Fig.6a, b). The maximum center move essentially westward, implying downstream eddy movement from winter to spring. The observed westward tendency is more significant than the simulated one. Strong mesoscale signals in the altimetric measurements could reach 14°N to the east of Vietnam. In the western SCS, MV within the southern band turns much weaker and its propagation speed is low at latitudes 5°N–15°N (Fig.4c, d and Fig.6). With weak mean flow and eddy activity, westward propagations prevail in the eastern and central basins.

In summer, the southwesterlies are blocked by the Annam Cordillera and accelerated to form a wind jet near 10°N (Xie et al., 2003). The resultant wind stress curl (WSC) dipole drives a strong anticyclonic gyre to the south and a weak cyclonic gyre to the north, with an eastward offshore jet near 11°N (Fig.7c, d). Along the northern band, the mean flow turns eastward, slowing down the MV propagations. At the same time, the mesoscale fluctuations reduce substantially and form high-variance patches rather than a continuous band (Fig.7a, b). In the western SCS, both observations and simulations show conspicuous MV near 11°N, which represents the variations of the offshore jet in response to intraseasonal wind pulses via Rossby wave adjustment (Xie et al., 2007). Affected by the offshore jet and the quasi-stationary anticyclonic gyre, the propagation pattern southeast off Vietnam is complex and lack of coherence (Fig.4c, d and Fig.7). From observations, another high MV area exists by 14°N, which is not reproduced in the OFES.

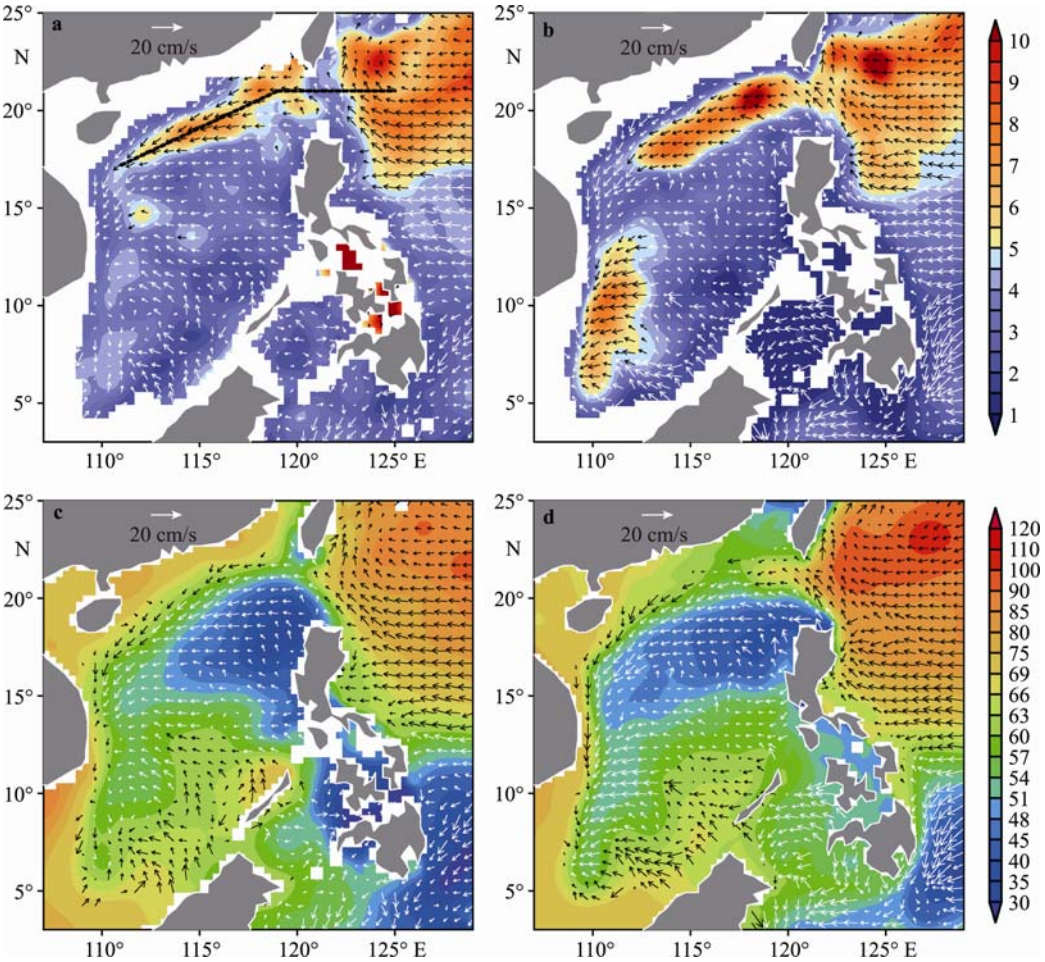

Fig.5 The standard deviation of sea level mesoscale signals (color shading, unit: cm) and propagation velocities of the signals (vectors) in winter: (a) altimeter observations and (b) OFES simulations. (c) The same vectors as (a) superimposed on the winter mean ADT (unit: cm). (d) The same vectors as (b) superimposed on the winter mean SSH from OFES (unit: cm)

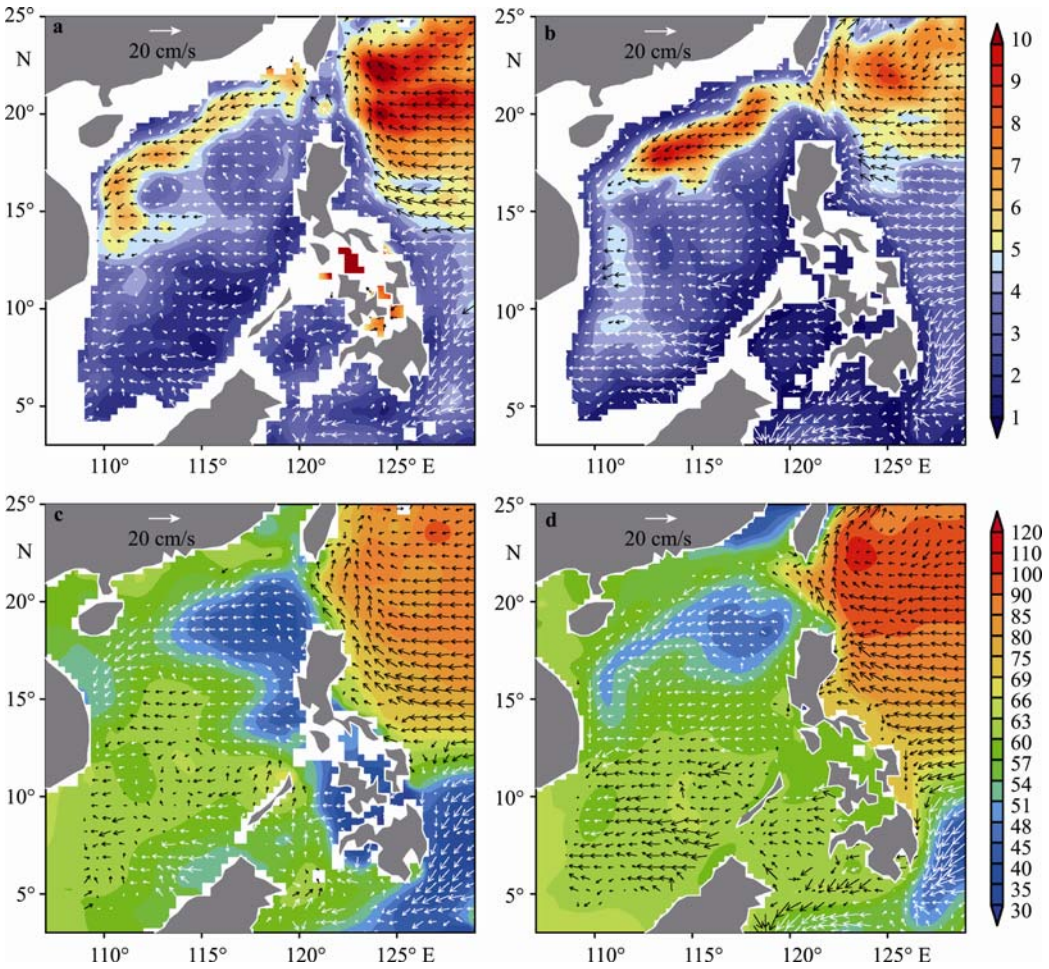

Fig.6 The standard deviation of sea level mesoscale signals (color shading, unit: cm) and propagation velocities of the signals (vectors) in spring: (a) altimeter observations and (b) OFES simulations. (c) The same vectors as (a) superimposed on the spring mean ADT (unit: cm). (d) The same vectors as (b) superimposed on the spring mean SSH from OFES (unit: cm)

The area features variability in frequency lower than that along the offshore jet to the south (figure not shown), which is possibly due to remnant eddy energy from the northern band during spring and/or the MV propagations from the east.

The monsoon transition from summer to winter regimes starts in the NSCS. The mean northeasterly occupies the northern basin during autumn, resulting in strong positive WSC in the north and weak positive WSC in the south of SCS. In response to the surface WSC, the mean circulation exhibits a cyclonic gyre north of 10°N (Fig.8c, d). South of the NSCS continental slope, the mesoscale signals grow in amplitude and their propagating speeds accelerate westward (Fig.8a, b). In the western SCS, the southern high-variance band becomes the most active and is oriented in an approximately meridional direction between 6°N to 13°N. The most striking feature is the nearly southward MV propagation along the southern band, which is inconsistent with local northeastward mean flow near 10°N–11°N. This unique southward eddy motion suggests that the potential vorticity dynamics for the generation of inertial recirculation are probably at work. Due to the asymmetric WSC pattern in the meridional direction, the vorticity input is much larger in the northern basin than in the southern part. With the effect of nonlinearity, the vorticity transports of the western boundary current generate southward recirculations and finally form detached eddies. This inertial recirculation theory is presented nicely in Bryan (1963). The detached eddies go on propagating southward, similar to the arrested topographic wave (Csanady, 1978). The amplitude of MV decreases southward remarkably suggesting decay of eddies being a result of smaller Coriolis force in lower latitudes.

To validate the reliability of the estimated vectors, Hovmöller diagrams of mesoscale signals along high-MV bands are plotted. The case in 2004–2005

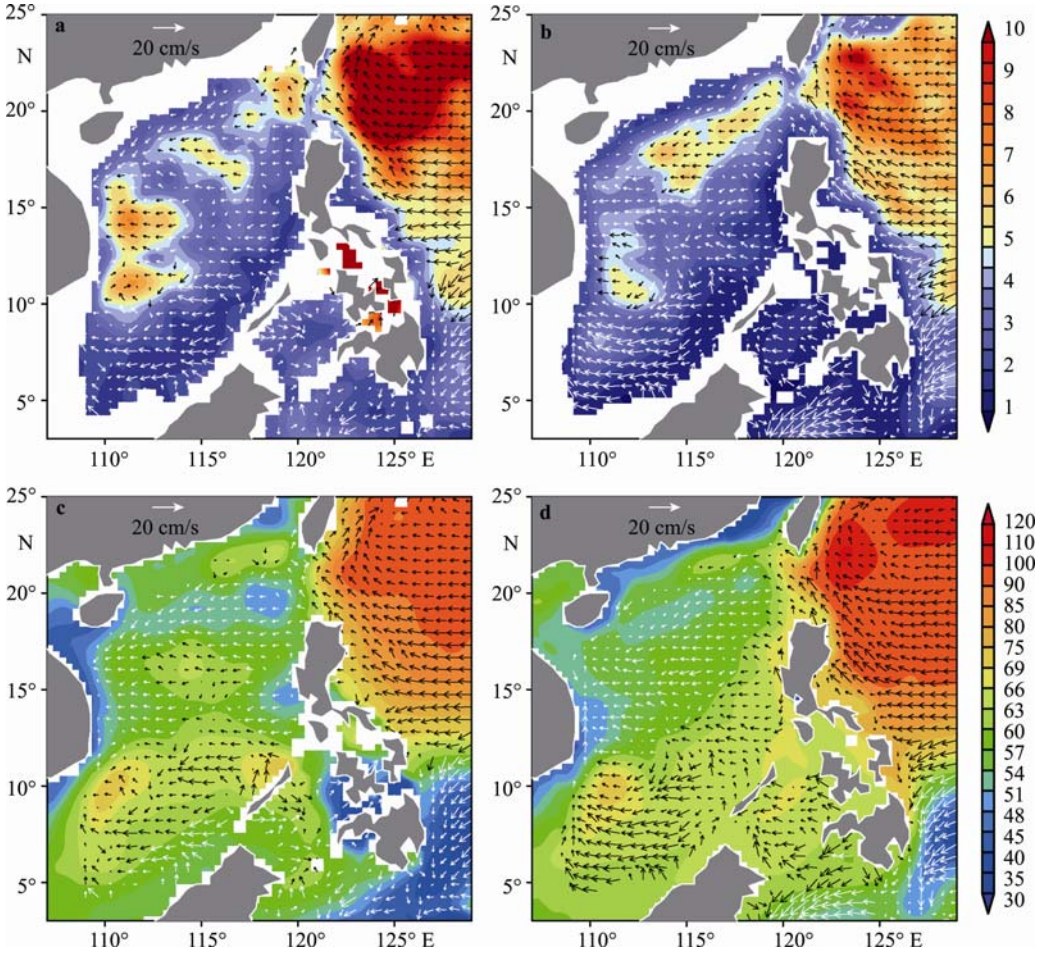

Fig.7 The standard deviation of sea level mesoscale signals (color shading, unit: cm) and propagation velocities of the signals (vectors) in summer: (a) altimeter observations and (b) OFES simulations. (c) The same vectors as (a) superimposed on the summer mean ADT (unit: cm). (d) The same vectors as (b) superimposed on the summer mean SSH from OFES (unit: cm)

displays substantial westward eddy movements along the northern band, with larger amplitudes from winter to spring (Fig.9a). Strong eddies are often generated near the Luzon Strait in winter and migrated to the vicinity of the western boundary during spring. Similar propagations with lower amplitude could be seen from summer to autumn. Seasonal variations of eddy propagation speed along the northern band (Fig.4a, b) suggest possible effects of mean flow advection. Fig.10 shows simulated flow velocity along the northern band averaged in zone of 111°E–119°E. The mean flow is northeastward in summer, strongly southwestward in winter, and moderately southwestward in spring and autumn, in accordance with the seasonality of eddy propagation speed. However, seasonal variability of eddy propagation speed is much weaker than that of surface mean flow, in agreement with previous observations, suggesting that eddy propagation velocity is several times less than the surface velocity of mean flow (Fu, 2006). The vertical flow shear is larger in autumn than in spring. Thus in water depth above 127 m, the westward mean flow is stronger in autumn, and beneath this depth, the current velocity becomes larger in spring. The higher eddy propagation speed in spring indicates that mean flow below 127 m has stronger impact on eddy movements. During summer, the mean flow turns northeastward, but the eddy propagation remains southwestward, albeit at reduced speeds. Such an all-year-round southwestward eddy propagation suggests that eddy motions along the northern band are dominated by wave propagation. Mean flow advection plays a secondary role in reducing the speed from about 8.5 cm/s in winter to nearly 5 cm/s in summer.

Along the southern band, a latitude-time diagram shows that the southward eddy propagations exist mainly in autumn rather than other seasons (Fig.9b). Comparing Fig.6 with Fig.8, we could see that to the

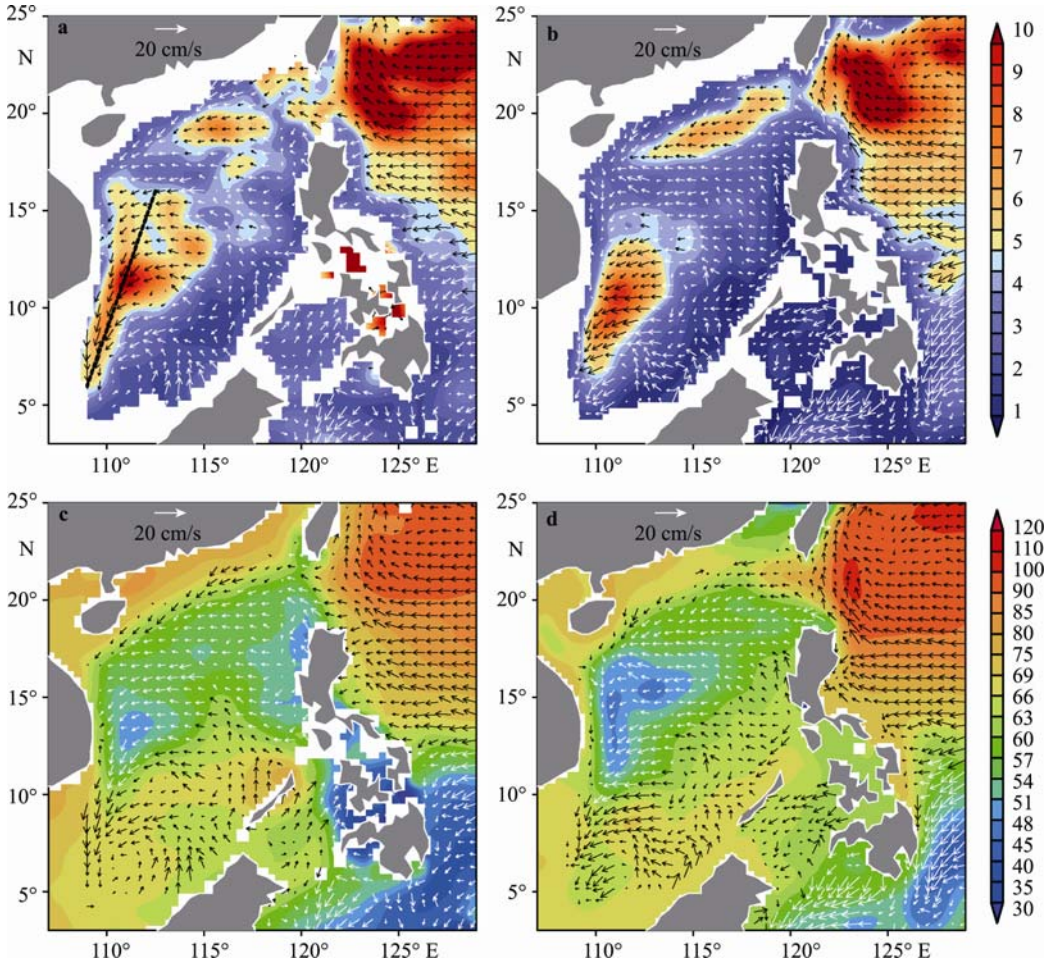

Fig.8 The standard deviation of sea level mesoscale signals (color shading, unit: cm) and propagation velocities of the signals (vectors) in autumn: (a) altimeter observations and (b) OFES simulations. (c) The same vectors as (a) superimposed on the autumn mean ADT (unit: cm). (d) The same vectors as (b) superimposed on the autumn mean SSH from OFES (unit: cm)

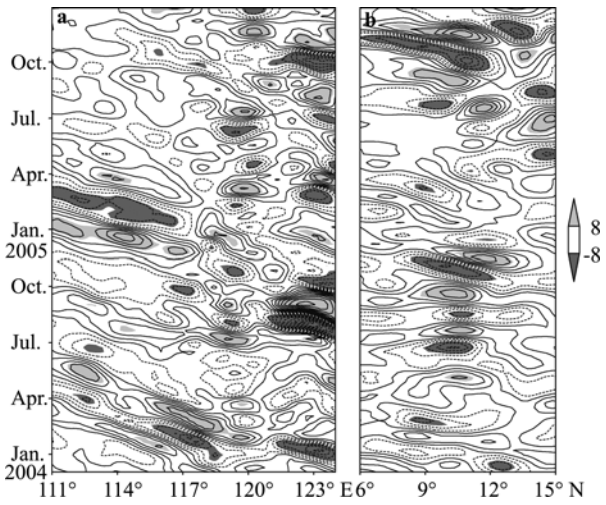

Fig.9 Hovmöller diagrams of observed SSH mesoscale signals (unit: cm) along two high-variance bands in the SCS: (a) longitude-time plot along the northern line shown in Figure 5a during 2004–2005; (b) latitude-time plot along the southern line shown in Figure 8a during 2004–2005

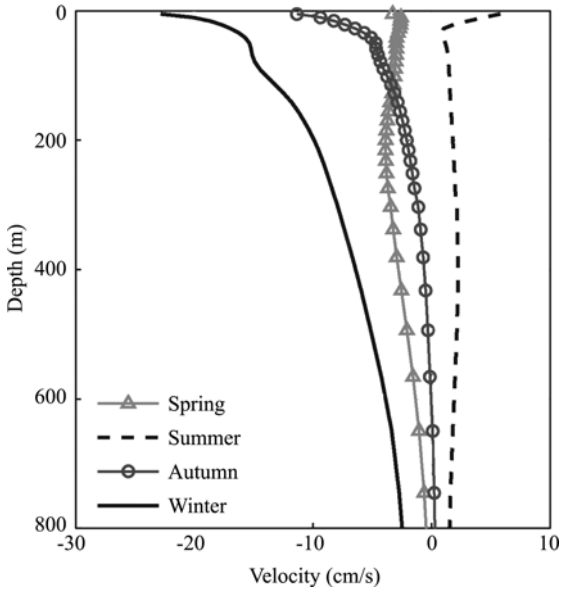

Fig.10 Flow velocities along the northern line shown in Fig.5a (averaged between 111°E and 119°E), based on OFES simulations

south of 10°N, the seasonal mean flows are weak in both spring and autumn. However, the southward eddy migrations are much more active in autumn, indicating that advection by mean flow has limited impact on the MV propagations along the southern band. We also note that eddy propagations in 2005 are more significant than that in 2004. The difference between the two years illustrates the significance of interannual variability, which deserves further study in the future.

4 DISCUSSION

The seasonal distributions of eddy kinetic energy (EKE) in the SCS were mapped in previous studies (Chen et al., 2009; He et al., 2002), which suggested a high-EKE spot east of Vietnam from summer to autumn and another one west of the Luzon Strait in winter. However, these results did not show high-EKE bands as identified in this study. The discrepancy can be attributed to different definitions of "eddy". In previous studies, seasonal signals on velocities were also treated as "eddy" variations, thus the EKE largely reflected a mixture of seasonal mean flows and transient eddies. In contrast, in a recent study focusing on intraseasonal sea level variations in the SCS, "eddy" was defined as the variability on intraseasonal timescales (Zhuang et al., 2010). The latter definition clearly displayed two high-energy bands, consistent with the two major eddy pathways revealed in this study. The contrast suggests that only after the removal of seasonal cycle will eddy pathways appear clearly.

In addition, in the eastern and central SCS, mesoscale signals mainly show westward propagation velocities, which are widely observed in the world oceans and attributed to the influence of baroclinic Rossby waves (Chelton et al., 2007; Morrow et al., 2004). Thus, the EKE generated west of the Luzon Island could transfer westward, resulting in weak local MV. It is noteworthy that few eddies can be generated south of 10°N due to weak Coriolis force and most of the mesoscale energy is probably propagating in the form of Rossby waves rather than eddies (Chelton et al., 2007). Thus, the pathways of MV adjacent to the Nansha Islands may not have been well detected because the local phase speed of Rossby waves is higher than 30 cm/s (Gan et al., 2001). This region exhibits very weak MV and is dynamically unimportant to this study.

5 CONCLUSION

In this study, pathways of oceanic mesoscale signals in the SCS are investigated using the MCC method. Both altimetry observations and model simulations exhibit two active MV bands. The northern band is formed by southwestward eddy propagations along 200–2 000 m isobaths south of the NSCS continental slope. The mesoscale signals are strong during the period from winter to spring and relatively weak in summer and autumn, in good agreement with local eddy occurrence rates (Wu et al., 2007). The southwestward eddy motions originate west of the Luzon Strait and exist throughout the year, indicating an intrinsic wave-propagation feature with steering effects of the bathymetry. The seasonality of mean flow plays a secondary role in modulating the propagating speed. With the aid of mean flow advections, the velocities of eddy motions reach a maximum in winter and a minimum in summer.

The southern MV band is located southwest off the Vietnam coast and oriented in an approximately meridional direction. Different from the propagation feature in the NSCS, the eddy movements along the southern band mainly occur in autumn, become weak in winter and disappear in spring and summer. The southward eddy pathway could not be explained by the advection of mean flow. The meridionally asymmetric WSC in autumn leads to the imbalance of vorticity inputs between the northern and southern basin. Vorticity transport by the western boundary current induces recirculation and eddy detachments through the inertial process, which is considered to be the mechanism of the southward eddy propagations. After arriving at lower latitudes in the form of an arrested topographic wave, the eddy decays faster due to the latitudinal dependency of Coriolis force.

Instead of the previous Lagrangian descriptions on the movement of individual eddies in the SCS (Wang et al., 2003b; Xiu et al., 2010), the space-time correlation analysis used in this study provides an Eulerian description of eddy pathways, which is important information for gaining further understanding of eddy dynamics. Despite discrepancies in magnitude, OFES reproduces both the observed MV and its propagation features quite well. Inter-comparison between observations and simulations validates not only the performance of OFES but also the reliability of MV propagations revealed by the MCC method.

6 ACKNOWLEDGMENTS

The altimeter products were produced by

SSALTO/DUACS and distributed by AVISO with support from CNES. The OFES simulation was conducted on the Earth Simulator under the support of JAMSTEC. The authors are grateful to two anonymous reviewers for their thoughtful comments on the manuscript.

References

Bryan K. 1963. A numerical investigation of a non-linear model of a wind-driven ocean. *J. Atmos. Sci.*, **20**: 594-606.

Carrère L, Lyard F. 2003. Modeling the barotropic response of the global ocean to atmospheric wind and pressure forcing - comparisons with observations. *Gephys. Res. Lett.*, **30**(6): 1 275, doi:10.1029/2002GL01647.

Chelton D B, Schlax M G, Samelson R M, de Szoeke R A. 2007. Global observations of large oceanic eddies. *Geophys. Res. Lett.*, **34**, L15606, doi:10.1029/2007 GL030812.

Chen G, Hou Y, Chu X, Qi P, Hu P. 2009. The variability of eddy kinetic energy in the South China Sea deduced from satellite altimeter data. *Chin. J. Oceanol. Limnol.*, **27**(4): 943-954.

Chu P C, Fan C W, Lozano C J, Kerling J L. 1998. An airborne expendable bathythermograph survey of the South China Sea, May 1995. *J. Geophys. Res.*, **103**: 21 637-21 652.

Csanady G. 1978: The arrested topographic wave. *J. Phys. Oceanogr.*, **8**: 47-62.

Domingues C M, Goncalves G A, Ghisolfi R D, Garcia C A E. 2000. Advective surface velocities derived from sequential infrared images in the southwestern Atlantic Ocean. *Remote Sens. Environ.*, **73:** 218-226.

Ducet N, Le Traon P Y, Reverdin G. 2000. Global high resolution mapping of ocean circulation from TOPEX/Poseidon and ERS-1/2. *J. Geophys. Res.*, **105**: 19 477-19 498.

Emery W, Thomas A C, Collins M J, Crawford W R, Mackas D L. 1986. An objective method for computing advective surface velocities from sequential infrared satellite images. *J. Geophys. Res.*, **91**: 12 865-12 878

Fu L L. 2006. Pathways of eddies in the South Atlantic Ocean revealed from satellite altimeter observations. *Geophys. Res. Lett.*, **33**, L14610, doi:10.1029/2006GL026245.

Fukumori I, Raghunath R, Fu L L. 1998. Nature of the global large scale sea level variability in relation to atmospheric forcing: A modeling study. *J. Geophys. Res.*, **103**: 5 493-5 512.

Gan J, Li H, Curchitser E N, Haidvogel D B. 2006. Modeling South China Sea circulation: Response to seasonal forcing regimes. *J. Geophys. Res.*, **111**: C06034, doi:10. 1029/2005JC003298.

Gan Z, Cai S. 2001. Geographical and seasonal variability of Rossby radii in South China Sea. *J. Tropical Oceanology*, **20**(1): 1-9. (in Chinese with English abstract)

He Z, Wang D, Hu J. 2002. Features of eddy kinetic energy and variations of upper circulation in the South China Sea. *Acta Oceanol. Sin.*, **21**: 305-314.

Hu J, Kawamura H, Hong H, Kobashi F, Wang D. 2001. 3~6 months variation of sea surface height in the South China Sea and its adjacent ocean. *J. Oceanogr.*, **57**: 69-78.

Jia Y, Liu Q, Liu W. 2005. Primary study of the mechanism of eddy shedding from the Kuroshio Bend in Luzon Strait. *J. Oceanogr.*, **61**: 1 017-1 027.

Li L, Nowlin W D, Su J. 1998. Anticyclonic rings from the Kuroshio in the South China Sea. *Deep-Sea Res. Part I*, **45**: 1 469-1 482.

Li L, Jing C, Zhu D. 2007. Coupling and propagating of mesoscale sea level variability between the western Pacific and the South China Sea. *Chin. Sci. Bull.*, **52**(12): 1 699-1 707.

Liu Q, Jia Y, Liu P, Wang Q. 2001a. Seasonal and intraseasonal thermocline variability in the central South China Sea. *Geophys. Res. Lett.*, **28**(23): 4 467-4 470.

Liu Z, Yang H, Liu Q. 2001b. Regional dynamics of seasonal variability in the South China Sea. *J. Phys. Oceanogr.*, **31**: 272-284.

Lyard F, Lefebre F, Letellier T. 2006. Modelling the global ocean tides: Modern insights from FES2004, *Ocean Dyn.*, **56**: 394-415.

Masumoto Y, Sasaki H, Kagimoto T, Komori N, Ishida A, Sasai Y, Miyama T, Motoi T, Mitsudera H, Takahashi K, Sakuma H, Yamagata T. 2004. A fifty-year eddy-resolving simulation of the world ocean-preliminary outcomes of OFES (OGCM for the earth simulator). *J. Earth Simulator*, **1**: 31-52.

Metzger E J. 2003. Upper ocean sensitivity to wind forcing in the South China Sea. *J. Oceanogr.*, **59**: 783-798.

Morrow R, Birol F, Griffin D, Sudre J. 2004. Divergent pathways of cyclonic and anti-cyclonic ocean eddies. *Geophys. Res. Lett.*, **31**, L24311, doi:10.1029/2004GL 020974.

Pascual A, Faugère Y, Larnicol G, Le Traon P. Y. 2006. Improved description of the ocean mesoscale variability by combining four satellite altimeters. *Geophys. Res. Lett.*, **33**, L02611, doi:10.1029/2005GL024633.

Pacanowski R C, Griffies S M. 2000. MOM 3.0 Manual. Geophysical Fluid Dynamics Laboratory/National Oceanic and Atmospheric Administration, 680p.

Qu T, Du Y, Gan J, Wang D. 2007. Mean seasonal cycle of isothermal depth in the South China Sea. *J. Geophys. Res.*, **112**, C02020, doi:10.1029/2006JC003583.

Richman J G, Wunsch C, Hogg N G. 1977. Space and time scales and mesoscale motion in the sea. *Rev. Geophys.*, **15**: 385-420.

Rio M H, Schaeffer P, Lemoine J M, Hernandez F. 2005. Estimation of the ocean Mean Dynamic Topography through the combination of altimetric data, in-situ measurements and GRACE geoid: From global to regional studies. *Proceedings of the GOCINA International Workshop*, Luxembourg.

Sasaki H, Sasai Y, Nonaka M, Masumoto Y, Kawahara S. 2006. An eddy-resolving simulation of the quasi-global

ocean driven by satellite-observed wind field: Preliminary outcomes from physical and biological fields. *J. Earth Simulator*, **6**: 35-49.

Schlax M G, Chelton D B. 1994. Aliased tidal errors in Topex/Poseidon sea surface height data. *J. Geophys. Res.*, **99**(24): 24 761-24 775.

Shaw P T. 1991. Seasonal variation of the intrusion of the Philippine Sea water into the South China Sea. *J. Geophys. Res.*, **96**: 821-827.

Volkov D L, Larnicol G, Dorandeu J. 2007. Improving the quality of satellite altimetry data over continental shelves. *J. Geophys. Res.*, **112**, C06020, doi:10.1029/2006JC 003765.

Wang D, Wang W, Shi P, Guo P, Gan Z. 2003a. Establishment and adjustment of monsoon-driven circulation in the South China Sea. *Science in China*, *Ser. D*, **46**: 173-191.

Wang G, Su J, Chu P C. 2003b. Mesoscale eddies in the South China Sea observed with altimeter data. *Geophys. Res. Lett.*, **30**(21): 2 121, doi:10.1029/ 2003GL018532.

Wang G, Chen D, Su J. 2008. Winter eddy Genesis in the eastern South China Sea due to orographic wind jets. *J. Phys. Oceanogr.*, **38**: 726-732.

Wang L, Koblinsky C J, Howden S. 2000. Mesoscale variability in the South China Sea from the TOPEX/ Poseidon altimetry data. *Deep Sea Res.*, *Part I*, **47**: 681-708.

Wu C R, Chiang T L. 2007. Mesoscale eddies in the northern South China Sea. *Deep Sea Res.*, *Part II*, **54**: 1 575-1 588.

Wyrtki K. 1961. Physical oceanography of the southeast Asian waters, Scientific results of marine investigations of the South China Sea and the Gulf of Thailand, NAGA Rep. 2. Scripps Inst. of Oceanogr., La Jolla, California. 195p.

Wyrtki K, Magaard L, Hager J. 1976. Eddy energy in the oceans. *J. Geophys. Res.*, **81**: 2 641-2 646.

Xie S P, Xie Q, Wang D, Liu W T. 2003. Summer upwelling in the South China Sea and its role in regional climate variations. *J. Geophys. Res.*, **108**(C8): 3 261, doi:10. 1029/2003JC001867.

Xie S P, Chang C H, Xie Q, Wang D. 2007. Intraseasonal variability in the summer South China Sea: Wind jet, cold filament, and recirculations. *J. Geophys. Res.*, **112**: C10008, doi:10.1029/2007JC004238.

Xiu P, Chai F, Shi L, Xue H, Chao Y. 2010. A census of eddy activities in the South China Sea during 1993-2007. *J. Geophys. Res.*, **115**: C03012, doi:10.1029/2009JC00 5 657.

Xu X Z, Qiu Z, Chen H C. 1982. The general descriptions of the horizontal circulation in the South China Sea. *In*: Proceedings of the 1980 Symposium on Hydrometeorology of the Chinese Society of Oceanology and Limnology, Sci. Press, Beijing. p. 137-145. (in Chinese)

Yuan D, Han W, Hu D. 2006. Surface Kuroshio path in the Luzon Strait area derived from satellite remote sensing data. *J. Geophys. Res.*, **111**: C11007, doi:10.1029/ 2005JC003412.

Zhuang W, Xie S P, Wang D, Taguchi B, Aiki H, Sasaki H. 2010. Intraseasonal variability in sea surface height over the South China Sea. *J. Geophys. Res.*, **115**: C04010, doi:10.1029/2009JC005647.